# Use of half-cylinder obstacle for enhancing aeroelastic energy harvesting

Junlei Wang[1,2], Linfeng Geng[2], Abdessattar Abdelkefi[3], Daniil Yurchenko[4], Zhien Zhang[5,*], Kai Yang[6,*]

[1] *State Key Laboratory of Hydraulic Engineering Simulation and Safety, Tianjin University, Tianjin 300000, China*
[2] *School of Mechanical and Power Engineering, Zhengzhou University, Zhengzhou 450000, China*
[3] *Department of Mechanical and Aerospace Engineering, New Mexico State University, Las Cruces, NM, USA*
[4] *Institute of Mechanical, Process & Energy Engineering, Heriot-Watt University, Edinburgh EH14 4AS, UK*
[5] *Department of Chemical and Biomedical Engineering, West Virginia University, Morgantown, WV 26506, USA*
[6] *School of Aerospace Engineering, Huazhong University of Science and Technology, Wuhan 430074, China*

[*]Corresponding authors. Email: zhien.zhang@mail.wvu.edu; kaiyang@hust.edu.cn

**Abstract**

This study aims to improve the performance of the galloping-based piezoelectric energy harvester (GPEH) by benefiting from two half-cylinder obstacles. Two half-cylinder obstacles are employed to construct a variable cross-section tube which changes the airflow characteristics near the GPEH placed inside. The performance of the GPEH in the variable cross-section tube is tested by wind tunnel experiments. The experimental results show that compared with the traditional GPEH, the cut-in speed of the GPEH with the two half-cylinder obstacles at the downstream position -1.5*D* is reduced by 43.87%, from 2.23 m/s to 1.55 m/s. For the highest experimental wind speed of 4.29 m/s, the output voltage of the GPEH with the two half-cylinder obstacles is increased by 109.28 %, from 4.31 V to 9.02 V. Moreover, the performance of the GPEH with the obstacles can be improved by appropriately increasing the obstacle curvature and reducing the throat width. The computational fluid dynamics (CFD) simulations are conducted to qualitatively interpret the experimental discoveries. The results demonstrated that the downstream area is beneficial to the GPEH, whereas the upstream area degrades the performance.

**Keywords:** Wind energy; piezoelectric beam; galloping; half-cylinder obstacle; wind tunnel experiment

## 1. Introduction

Environmental energy harvesting technology has been developed rapidly in recent decades for its cleaning and renewable. For example, solar photovoltaic cells are widely used in daily heating, lighting and aerospace fields [1, 2], wind turbines are arranged in high wind speed areas to harvest wind energy for power generation [3, 4], and multi stage utilization of waste heat recovery [5]. Different types of environmental energy harvest devices are used in different fields due to the constraints of operating conditions and structure. Flow-induced vibration energy harvester (FIVEH) is a kind of micro environmental energy harvesting device based on the principle of flow-induced vibration (Vortex-induced vibrations [6, 7], Galloping [8, 9], Flutter [10, 11], etc.). It is mainly used to supply power for wireless sensor networks, micro electro mechanical systems and other small energy consuming devices [12, 13].

The FIVEH is usually realized by utilizing mechanical-electric converting principles such as piezoelectric [14], electromagnetic [15], electrostatic [16], and triboelectric [17], or the combinations [18]. Owing to the potential of harvesting the low-speed flow energy and high energy density, the FIVEH with piezoelectric devices have been studied intensively [19, 20]. For example, Abdelkefi et al. [21] constructed a galloping-based piezoelectric energy harvester (GPEH), and studied the influence of the Reynolds number of the incoming flow and the circuit load on the cut-in speed and energy harvesting efficiency of the GPEH. Javed et al. [22] established the mathematical model of the GPEH by using the distributed-parameter method, and studied the influence of different aerodynamic expressions on the output response of the GPEH. Due to the size limitations of the GPEH, the power output of micro-GPEH can only make the small sensor operate intermittently, which cannot guarantee the continuous operation of electrical equipment. How to improve the output power of the GPEH and make it adapted to the varied operate conditions has been a hot topic in the research of flow-induced vibration energy harvesting [23-25].

At present, the improvement of the GPEH mainly includes increasing magnetic field structure, improving the flow characteristics around bluff body, and optimizing the electrical circuitry. For example, Bibo et al. [26] and Alhadidi et al. [27] constructed a GPEH with magnetic field, and compared the

performance of the GPEH under different magnetic forces (softening, hardening, bi-stable). Wang et al. [28] analyzed the vibration characteristics and energy harvesting performance of GPEH with tri-stable structure under different wind speeds and resistance loads. Yang et al. [29, 30] constructed a double-beam piezo-magneto-elastic wind energy harvester (DBPME-WEH), established the electromechanical coupling model through Lagrange equation, and analyzed the influence of system's parameters and wind speed on its performance. Zhao et al. [31] and Lan et al. [32] analyzed the influence of different types of load circuit interface (AC, DC, SCE, SSHI) on the GPEH. In addition, to enhance the fluid-structure interaction for performance improvement of the GPEH, multiple methods were proposed to modify the aerodynamic force on bluff body, e.g., changing the shape of bluff body [33-35] and adding accessories on the surface of bluff body [36, 37].

Because the aerodynamic coefficient is closely related to the shape and surface of bluff body, the amplitude and frequency of the bluff body can be changed or the vibration mode can be changed by modifying the structure of bluff body. Yang et al. [38] analyzed the performance of the GPEH with different cross sections (D-section, square, triangle, and rectangle) for the wind speed range of 0-8 m/s. The GPEH with square cross-section has higher energy harvesting efficiency, and the maximum output power can reach 8.4 mW. Wang et al. [39] constructed a hybrid piezoelectric energy harvester coupled galloping and VIV by changing the shape of bluff body (the bluff body is composed of square column and cylinder). Their results showed that when combination angle of the bluff body is 90 degrees, the hybrid piezoelectric energy harvester has the advantages of GPEH and vortex-induced vibrations energy harvester (VIVPEH), and the maximum output voltage is 15.1% higher than that of the GPEH and 79.62% higher than that of the VIVPEH. Hu et al. [40] proposed a GPEH with two small attachments on bluff body, and analyzed the influence of attachment position on the GPEH. The results showed that the GPEH performed better when the attachment was at 45° and 60° positions.

The previous studies uncovered the physical connotation that the key of GPEH enhancement is to improve the vibration strength of an elastic structure driven by the unsteady aerodynamic force. It should be mentioned that in the past studies, the enhancement of unsteady aerodynamic force is mostly achieved by changing the structure of the bluff body, rarely by changing the intensity of flow field directly. On the other hand, GPEH is usually designed to work outdoors and a certain threshold wind speed is needed to arouse the galloping behavior. Addition to the previous methods that change the GPEH structure, an alternative can be used to enhance the performance by varying the airflow characteristics around the GPEH through adding obstacles. Abdelkefi et al. [41] innovatively proposed to place a circular cylindrical obstacle upstream of the conventional GPEH to enhance energy harvesting. The results reveal that the wake effect of the upstream obstacle can greatly broaden the speed range of energy harvesting, and the degree of enhancement depends on the distance between the upstream obstacle and the downstream bluff body. Recently, Zhang et al. [42, 43] added a fixed interference obstacle downstream of VIVPEH to enhance energy harvesting performance. Their results show that the plate interference obstacle for the energy harvester has a superior harvesting performance than the cylindrical obstacles. Wang et al. [44] further studied the influence of the placement and dimension of the downstream interference rectangular plate on the performance of VIVPEH. The results revealed that the optimal design scheme is to place a $2D$-high plate at $0.2D \sim 0.4D$ downstream of the bluff body. Furthermore, Yan et al. [45] proposed a tandem configuration of energy harvester with interference from upstream and downstream obstacles. The results present that the upstream spacing has a greater impact than the downstream spacing. Fan et al. [46] investigated the FIV characteristics of three flexible cantilever cylinders arranged in series, side-by-side and staggered arrangements. The potential of flexible multi-cylindrical wind energy harvesting is discussed, and the highest power harness efficiency can reach 52%. Nevertheless, the above-mentioned studies on adding obstacles to enhance aerodynamic instability focused on the mutual interference between multiple cylinders, the internal influence mechanism of which is complex and cannot be easily controlled.

Inspired by the physical phenomenon of the flow dynamics of the variable cross-section tubes formed by obstacles [47], this study presents a novel concept of the galloping-based wind energy harvester using two half-cylinder obstacles to form a variable cross-section tube, which has not been reported before. This methodology achieves the concentration effect of wind energy by modifying the airflow features around the GPEH to significantly improve the aero-instability. Therefore, it is more like a wind energy concentrator and easier to control, which is far different from previous studies that focused on the GPEH structure and the mutual interference of multiple bluff bodies. When a low-Mach inlet wind enters the variable cross-section tube, its velocity would be significantly increased along with the narrowed tube cross-section area [47], leading to the concentration of wind energy and enhancement of the aerodynamic force. Thus, owing to the enhanced aerodynamic force, vibration of the GPEH placed near the tube throat might be substantially stronger, providing higher electrical power output. Note that, since the variable cross-section tube changes the airflow around the GPEH, it could be suitable for various types of the GPEH structures. Therefore, this study can enlighten a new path of effectively improve GPEH performance.

The rest of this paper is organized as follows: section 2 presents the concept of the GPEH with the two half-cylinder obstacles (which forms a variable cross-section tube), where the experimental prototype of the system in a wind tunnel is shown. Section 3 presents the results of the wind tunnel experiments to study the effect of the variable cross-section tube upon the existing design guidelines for GPEH performance improvement. The CFD simulations based on the Lattice-Boltzmann method (LBM) are conducted in section 4 to qualitatively interpret the performance improvement.

## 2. Concept of GPEH with two half-cylinder obstacles

**Fig**. **1**(a-c) presents the 3D sketch, experimental prototype, and top view of the GPEH in the variable cross-section tube formed by two half-cylinder obstacles, respectively. **Fig**. **1** shows that the two half-

cylinders form the variable cross-section tube, which changes the airflow characteristics around the GPEH. Position 0*D* indicates the tube throat where the tube has the narrowest width, between the inlet and outlet in **Fig. 1**(c). The left and right sides of the throat are upstream and downstream areas, respectively. The GPEH comprises a cantilever piezoelectric beam and a cuboid bluff body. Due to the fluid-structure interaction between the cuboid bluff body and the incoming airflow, the piezoelectric beam will exhibit the galloping phenomenon when the wind speed around the bluff body is greater than a cut-in speed. The galloping consequently generates electric power through the piezoelectric transduction mechanism. The experiments are conducted in an open-circuit circular-section wind tunnel. The parameters of the prototypes are presented as follows. The beam material is the pure aluminum, the piezoelectric transducer material is PZT-5 (Jiayeshi Co., China) with the internal capacitance of 11.2 nF, and the bluff body and obstacles are made of foam. The dimensions of the piezoelectric beam and bluff body are $L \times W \times h = 105 \times 25 \times 0.5$ mm$^3$ and $L_b \times D \times D = 118 \times 32 \times 32$ mm$^3$, respectively. The variable cross-section tube curvature and obstacle height are $K$ and $H$. The throat width is $L_g$ $L_g$. To eliminate the influence of the three-dimensional effect, the obstacle height is greater than the height of the bluff body. Moreover, considering the limited internal space and the efficiency of the experiment, $K$ = 6.7, 8, 10 and $L_g$ = 3.5$D$, 4.5$D$, 5.5$D$ were studied. It should be pointed out that the curvature $K$ is equal to the reciprocal of the radius of the circle. Obstacles are made by cutting circular cylinders with different radii. The radius of the circular cylinder used is 0.1, 0.125 and 0.15 m, and the corresponding curvature $K$ is 10, 8 and 6.7, respectively.

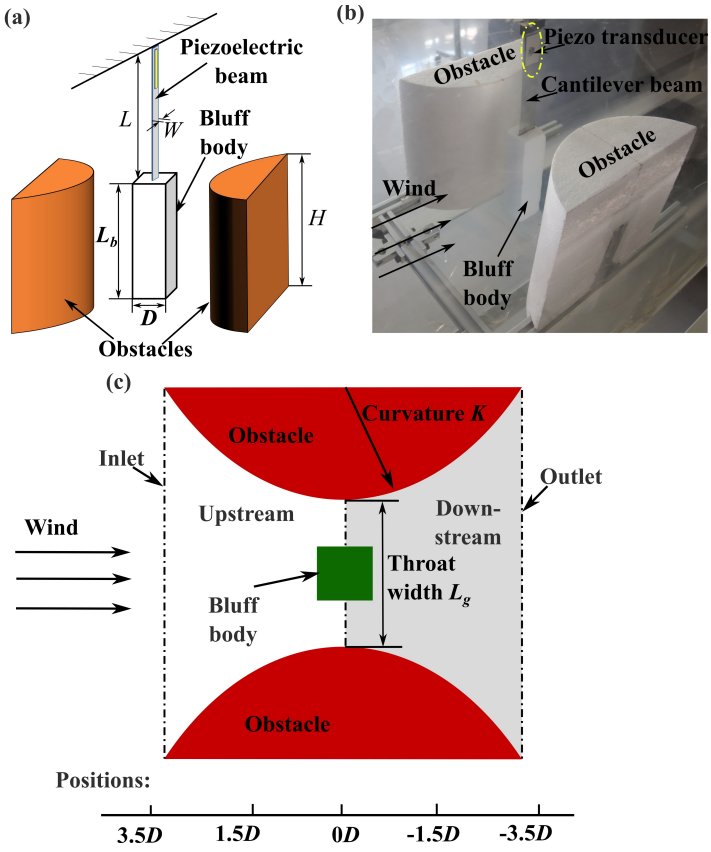


**Fig. 1** (a) 3D schematic, (b) experimental prototype, and (c) top view of the GPEH in the variable cross-section tube formed by the two obstacles.

## 3. Experimental results and discussion

### 3.1 Experimental setup

**Fig. 2** shows the comprehensive view of the wind tunnel testing platform. In this work, the wind tunnel for producing the incident air flow is with a round cross-section of the diameter of 400 mm. Two honeycomb sections are equipped to stabilize the incoming wind. The detailed parameters of the system and the fabricated physical prototype have been given in the previous sections. The wind speed is measured by a hot-wire anemometer (405i, Testo Co, USA), the output electrical signals are measured by a Data collector (DS1104S, RIGOL, China). The system damping ratio and natural frequency are measured by a free vibration experiment. The natural frequency and damping ratio of the piezoelectric beam along with the bluff body for its first mode are 8.23 Hz and 0.0267, respectively. The effective mass

of bluff body is 3.87 g. The operation wind speed of the wind tunnel in the following case study is beyond 1.0 m/s, the kinematic viscosity is $1.5\times10^{-5}$ at the temperature of 20°C. A series of wind tunnel tests under a low-turbulence flow with a turbulence intensity less than 0.01 are conducted to evaluate the actual performance of the proposed GPEH.

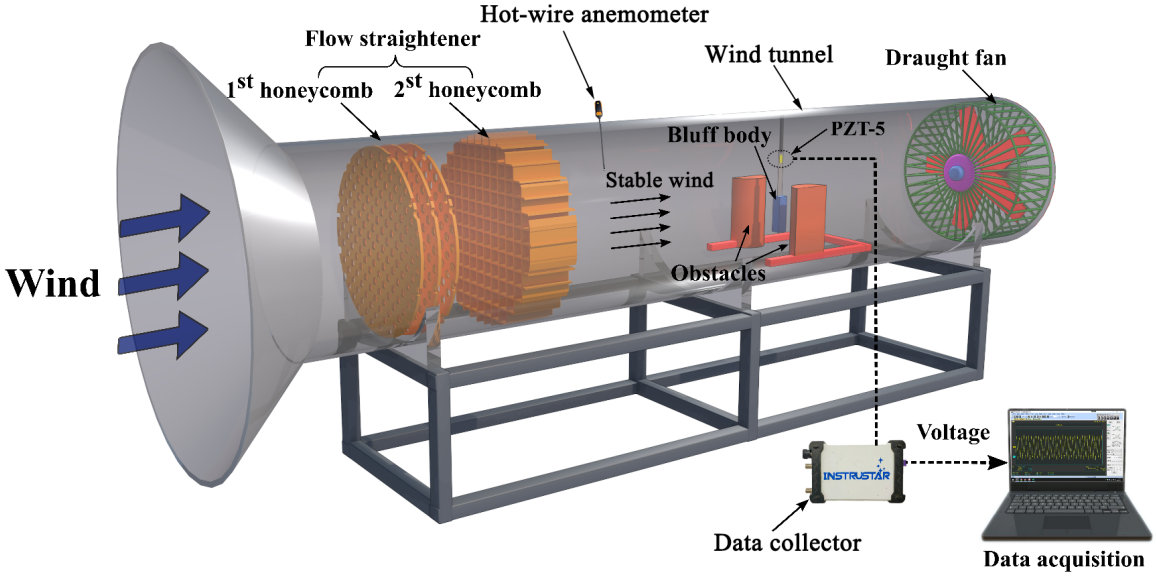


**Fig. 2** The entire view of the wind tunnel experimental setup.

### 3.2 The benefit of the half-cylinder obstacles for the GPEH performance enhancement

**Fig. 3** presents the comparison of root mean square (RMS) voltage output $V_{rms}$ of the GPEH with and without the obstacles for a range of the inlet wind speeds $U = 1.0$ m/s~ 4.5 m/s. In this figure, the GPEH is at the position of $-1.5D$ (which is in the downstream area). In this experiment, the parameters are $K$ =10 m$^{-1}$, $H = 0.2$ m, and $L_g = 4.5D$. The experimental results show that for both the cases, the GPEH's RMS voltage output becomes higher along with the increasing wind speed. However, the two curves have a significant difference in terms of the cut-in speed and the generated voltage's increasing rate. The cut-in speed of the GPEH with the two half-cylinder obstacles is 1.55 m/s, whereas the cut-in speed of the GPEH without the obstacles is 2.33 m/s. This indicates that the half-cylinder obstacles are more beneficial

to broaden the effective energy-harvesting wind range with lowering the onset speed of galloping. When the inlet wind speed is higher than 1.33 m/s, for each wind speed $U$, the GPEH in the variable cross-section tube formed by the two obstacles generates significantly higher $V_{rms}$ than the GPEH without the obstacles. For example, the GPEH with the obstacles produces $V_{rms} = 9.02$ V for the maximum inlet wind speed $U = 4.29$ m/s, which is 109.28 % of the $V_{rms}$ without the obstacles (4.31 V). In addition, it should be noted that when the wind speed $U = 4.29$ m/s, the vibration frequency of the GPEH with and without the obstacles are very close, but the time-domain voltage amplitude of the GPEH with the obstacles (12.33V) is much larger than that of without the obstacles (5.58V), as shown in Fig.4. The results indicate that owing to the two half-cylinder obstacles, the GPEH at the downstream position -1.5$D$ significantly outperforms the GPEH without the presence of the obstacles. The benefit of the downstream position of the variable cross-section tube for GPEH performance improvement is well established and will be qualitatively interpreted in the CFD studies in Section 4.

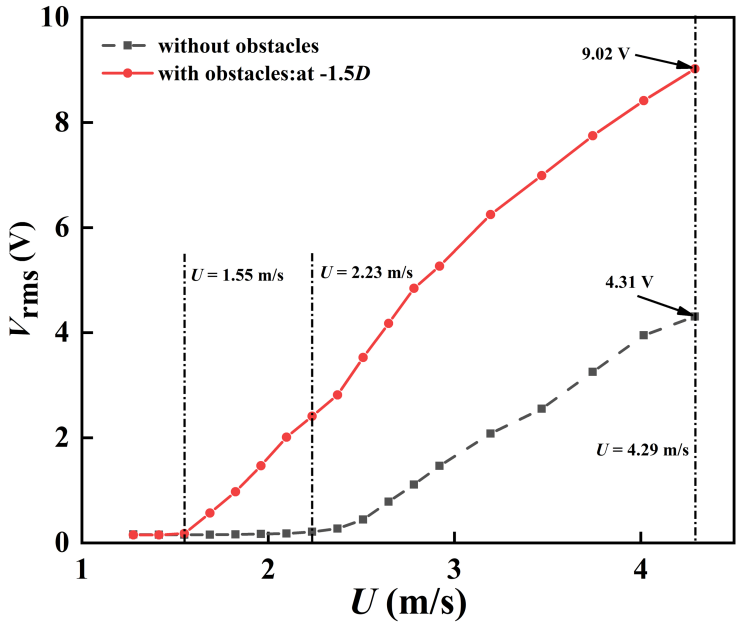


**Fig. 3** The RMS voltage outputs of the GPEH with and without the two half-cylinder obstacles for the inlet wind speeds $U$ = 1.28-4.29 m/s in the wind tunnel experiment.

The wind tunnel experiments are conducted to investigate the influence of different positions in the variable cross-section tube on the GPEH performance. **Fig. 4** presents the RMS voltage outputs of the GPEH at different positions in the downstream and upstream of the tube, respectively. The results of the GPEH without the obstacles are also presented as the benchmark in each figure. As shown in the plotted curves in **Fig. 4**, different positions of the GPEH in the tube saliently affect the energy harvesting performance. **Fig. 4**(a) shows that in the downstream area, the voltage outputs are enhanced for most wind speeds compared to the GPEH without the obstacles, the cut-in speed decreases from 2.23 m/s to 1.55 m/s, and the cut-in speed does not change along with the different positions. Meanwhile, for the wind speed of 4.29 m/s, the voltage outputs of the GPEH with the obstacles first increases and then decreases with the position increasing. The maximum output voltage reaches 9.38V at position -2.5*D*, which is 118.14% higher than that of the GPEH without the obstacles. It is possible that the velocity and pressure field of the airflow in the tube vary with the position of the variable cross-section tube. When the GPEH is at position -2.5*D*, the aerodynamic force acting on the bluff body is higher than that at other positions. Then, with the increase of the position, the influence of the obstacles on the flow field and pressure field around the GPEH gradually decreases, and its output voltage gradually decreases, which is close to that of the GPEH without the obstacles. However, the upstream area degrades the energy harvesting performance by decreasing the voltage outputs, as indicated in **Fig. 4**(b). The voltage output decreases first and then increases when the position is increased. The output voltage is 0.75 V at 2.5*D* for the wind speed of 4.29 m/s, which is far lower than that of the GPEH without the obstacles. It should be noted that at position 1.5 *D* and 2.5*D*, the cut-in speed of the GPEH is 3.47m/s and 3.74m/s respectively, which is unfavorable for energy harvesting. The results indicate that to realize the optimal energy harvesting performance, the GPEH should be placed in the downstream area of -1.5*D* and -2*D*. The discovered experimental phenomena will be explained later in section 4.

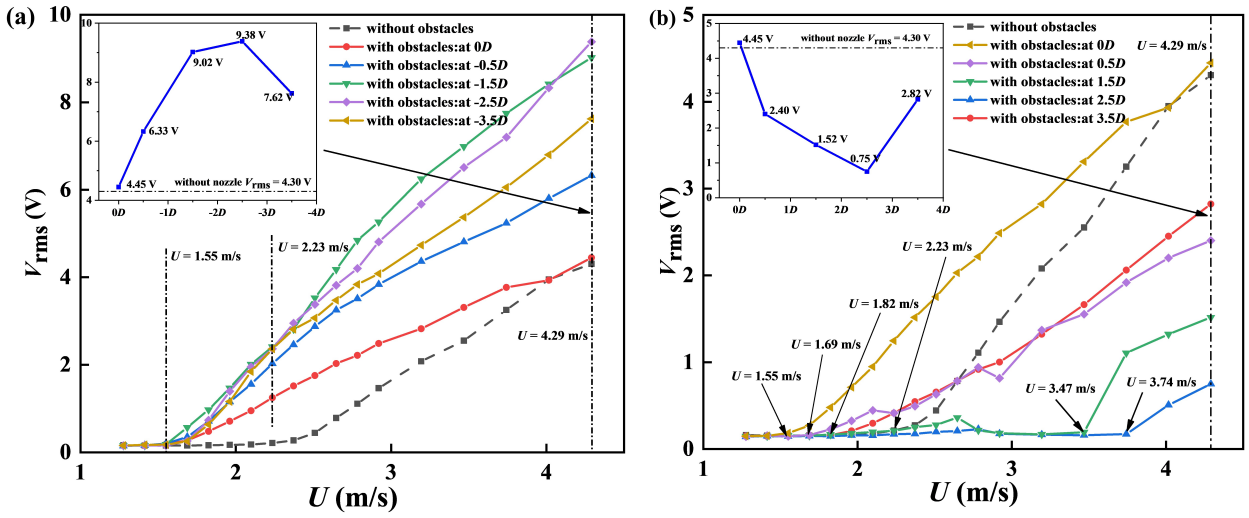


**Fig. 4** The RMS voltage output of the GPEH: (a) in the downstream area: [0$D$, -0.5$D$, -1.5$D$, -2.5$D$, -3.5$D$] and (b) the upstream area: [0.5$D$, 1.5$D$, 2.5$D$, 3.5$D$].

### 3.3 The effective design guideline of the half-cylinder obstacles for the GPEH

To develop insights into the effective design of the half-cylinder obstacles for the GPEH performance improvement, the following experiments are performed. **Fig. 5**(a-b) shows the RMS voltage outputs of the GPEH corresponding to three different obstacle curvatures $K$ at the position -1.5$D$ for the throat width $L_g = [3.5D, 4.5D]$, respectively. Results show that, for both $L_g = 3.5D$ and $4.5D$, the variation trends of the RMS voltage output corresponding to the curvatures are similar. That is, increasing the obstacle curvature leads to higher voltage output. At the same time, comparing the output voltage curves in **Fig. 5** (a) and (b), it can be found that when the throat width increases from 3.5$D$ to 4.5$D$, the cut-in speed of the GPEH does not change. For the wind speed of 4.29 m/s, the maximum output voltage at increases from 8.32 V to 9.02 V. It should be noted that the larger obstacle curvature $K$ leads to a higher difference in the flow areas between the inlet and the outlet. The significant difference of the flow areas would accelerate the local wind speed near the GPEH bluff body. Consequently, this produces a stronger galloping of the GPEH, leading to the higher voltage output.

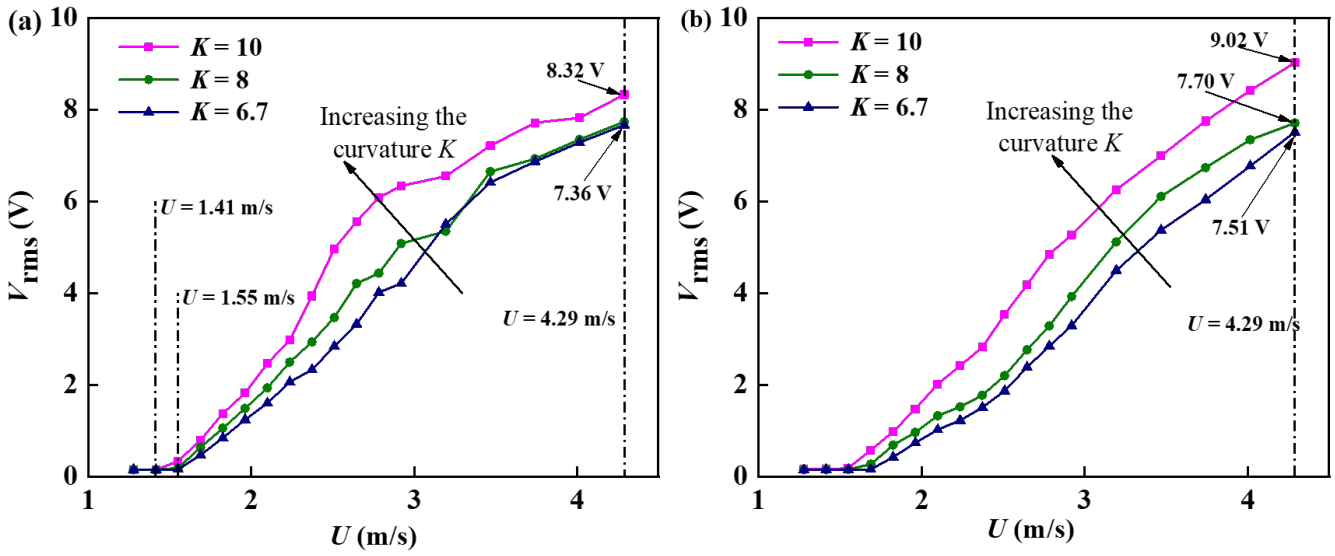


**Fig. 5** The experimental RMS voltage output of the GPEH corresponding to different obstacle curvatures $K = [6.7, 8, 10]$ mm at the position -1.5$D$ for: (a) $L_g = 3.5D$ and (b) $L_g = 4.5D$.

It can be seen that the principle of the Laval nozzle is to increase the flow-area difference of the inlet and the throat for improving GPEH galloping vibration. Thus, apart from increasing the obstacle curvature, another possible measure is to change the throat width $L_g$ of the tube. The effectiveness of this measure is proved experimentally by the results shown in **Fig. 6**(a-c) where three different $L_g$ values are set to investigate the GPEH performance at the position $-1.5D$ for the curvatures of each obstacle, namely, $K = 6.7$, $K = 8$, and $K = 10$. The results show that for each curvature, reducing $L_g$ to narrow the tube leads to voltage output improvement of the GPEH for a wide range of the inlet wind speeds when $U \leq 3.74$ m/s. For the wind speed exceeds 3.74 m/s, the GPEH with the throat width $L_g = 4.5D$ shows a better prospect of energy harvesting. It should be mentioned that while narrowing the tube is beneficial to energy harvesting performance at low wind speeds, the bluff body of the GPEH may likely collide with the obstacles during vibration. This may restrict the vibration amplitude of the GPEH. Thus, there is a trade-off between narrowing down the tube cross-section for improving energy harvesting performance and offering the sufficient room for the vibrations of the GPEH to occur.

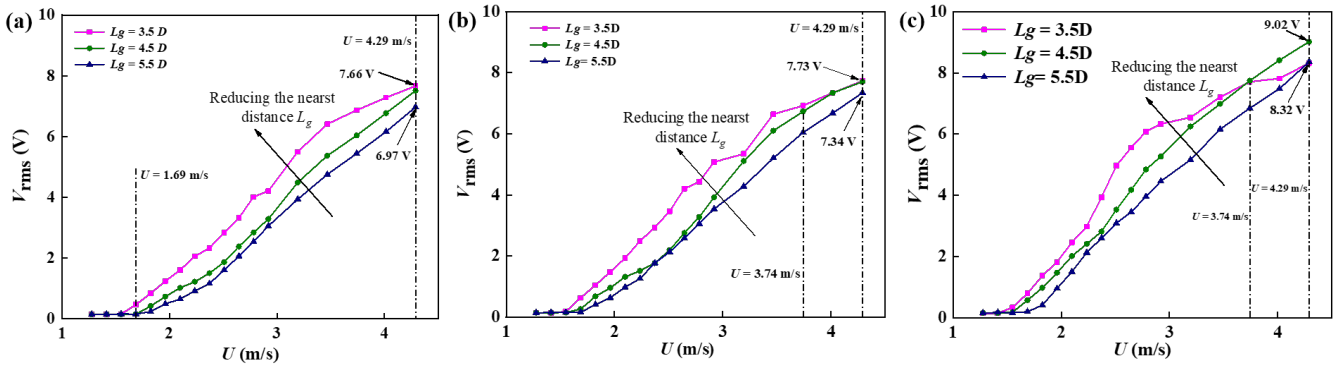


**Fig. 6** The RMS voltage output of the GPEH corresponding to different throat widths: $L_g = [3.5D, 4.5D, 5.5D]$ at the position -1.5$D$ for the curvatures: (a) $K = 6.7$, (b) $K = 8$, and (c) $K = 10$.

## 4. Qualitative interpretation using CFD

Since the bluff body volume is comparable to the Laval nozzle width, there will exist a complex fluid-structure interaction between the nozzle walls, bluff body, and a wind pattern in the nozzle. This will exhibit a different fluid dynamic phenomenon from the case where there is no bluff body in the nozzle. Due to the complex fluid-structure interaction, it is quite difficult to formulate a theoretical model to describe the fluid distribution of the investigated case. Therefore, the computational fluid dynamics (CFD) simulations are employed to better understand the flow characteristics in the Laval nozzle structure. The comprehensive two-dimensional flow passing bluff bodies CFD simulations are conducted on the XFlow [39, 48], a Lattice-Boltzmann (LBM) principle-based platform (Dassault co., Paris, France). The flow field distribution can be accurately solved by a No-Meshing method based on the D2Q9 lattice collision model. It can also be illustrated that the airflow acceleration happens in the Laval nozzle and the highest velocity gradient occurs at the throat position of the nozzle [47]. In this work, however, a cuboid-bluff body is equipping in the nozzle that will dramatically change the flow distribution in the nozzle. Thus, it is important to investigate the optimal position for enhancing the performance of GPEH. The authors had proved the superiority of LBM in previous studies [39, 48]. Different from the traditional finite volume method (FVM) [49] and finite difference method (FDM) [50], the LBM does not directly solve the

complex Navier-Stokes equation, but obtains the macroscopic behavior of the fluid by calculating the collision and migration of discrete particles. Therefore, the LBM adopts a simpler description of fluid interaction, which is very suitable for analyzing the complex fluid-structure interaction. The calculation domain in this paper is a rectangular calculation domain with length and width of 60$D$ and 30$D$ respectively, where $D$ is the side length of square cylinder bluff body. The square cylinder bluff body is located on the central axis of the calculation domain and is 20$D$ and 40$D$ away from the upstream boundary and downstream boundary respectively. The downstream distance is much greater than the upstream distance to ensure the full development of vortex shedding behind the bluff body. The curvature $K$ of the obstacle is 10, the spacing $L_g$ = 4.5$D$, and the square cylinder is located on the symmetry axis of the obstacle. The boundary conditions are set as follows: the upstream boundary of the calculation domain is set as the velocity inlet boundary, the downstream boundary is set as the flow outlet boundary, the fluid attribute is air, and the other boundary conditions are set as the wall. At the same time, the flow mode is set as the external single-phase forced incompressible model, and the time step is 0.0001s.

**Fig. 7**(a-c) comprehensively shows the vortex shedding patterns of the GPEH at different positions in the nozzle within a time period $T_i$ ($i$=1,2,3), where $T_i$ are different Strouhal vortex shedding periods due to different positions of the bluff body. The nozzle parameters are $K$ =10 m$^{-1}$, $H$ = 0.2m, and $L_g$ = 4.5$D$. As shown in **Fig. 7**(a), for the bluff body at the position 1.5$D$ in the upstream of the nozzle, the local wind speed passing across the bluff body is low. The vortex shedding is quite regular and the "2S" vortex shedding pattern can be captured. Although a low-pressure region has been generated, which results in the large shedding vortex observed behind the nozzle outlet, it is far away from the GPEH bluff body. Consequently, the low pressure caused by the large shedding vortex does not enhance the vibration of the GPEH bluff body, which may not be favorable for wind energy harvesting. This can be used to explain that the output voltage of the GPEH at the upstream 1.5$D$ position observed in **Fig. 4**(b) is lower than that

of the traditional device. **Fig. 7**(b) shows that when the bluff body is placed at the throat (position 0*D*), the vortex shedding of the bluff body is significantly influenced by the nozzle due to the unevenly distributed pressure. The vortex shedding behind the bluff body is more rapid and irregular than that in **Fig. 7**(a), since the low-pressure region can attract the small vortex shedding from the bluff body. As a result, the low pressure strengthens the vibration of the GPEH bluff body at the throat, which corresponds to the experimental result at position 0*D* shown in **Fig. 4**. As shown in **Fig. 7**(c), when the GPEH is at the position -1.5*D* in the downstream, the low-pressure region exhibits a more stable form. The large vortex is attracted to the position behind the bluff body, which does not elapse. Attracted large vortices continuously provide the low-pressure region, and thus the vibration of the GPEH bluff body is significantly enhanced. The significant increase in the output voltage of the GPEH at the downstream -1.5*D* position observed in **Fig. 4**(a) reflects this fact. In addition, to comprehensively investigate the characteristics of the GPEH, the static pressure distribution and iso-contour of velocity around the bluff body and the Laval nozzle are further presented.

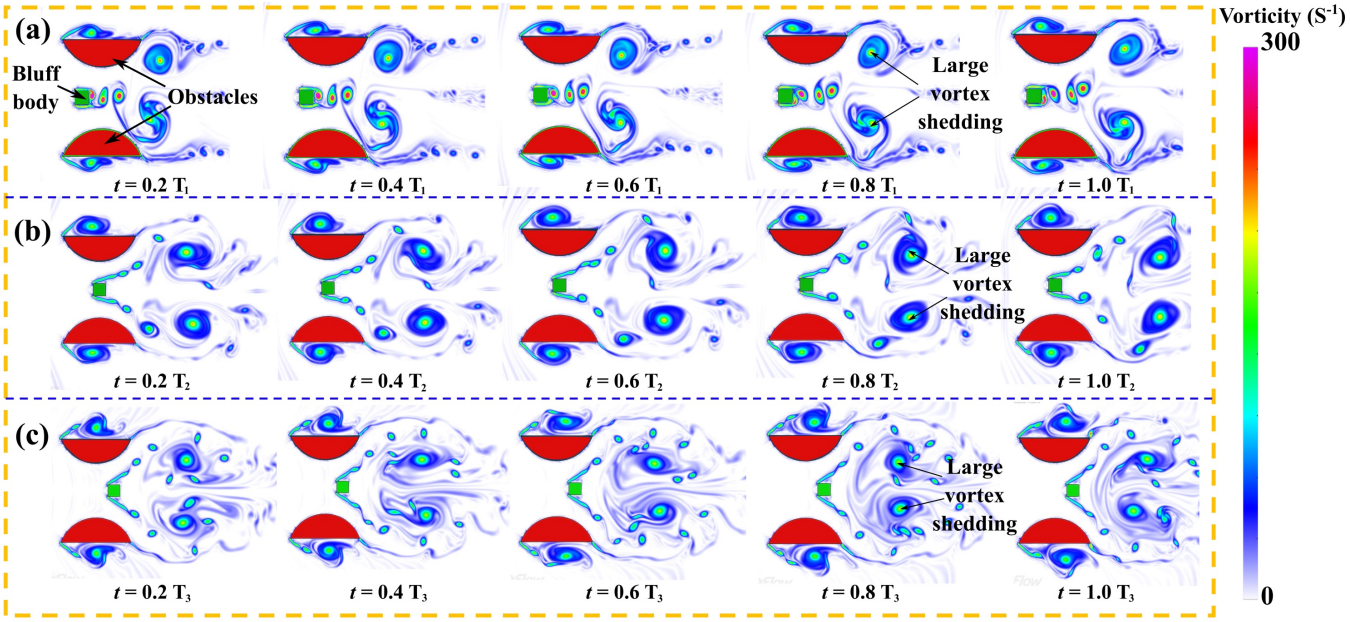


**Fig. 7** The comprehensive vortex shedding patterns of the GPEH in the Laval nozzle: (a) position 1.5*D* (upstream), (b) position 0*D* (throat), and (c) position -1.5*D* (downstream).

Besides, as shown in **Fig. 8** (a-c), low pressure region can be captured in the downstream behind the nozzle, which is formulated owing to the geometric topology of the Laval nozzle. Meanwhile, it can be indicated that in the low-pressure region the vibration could be influenced due to the pressure difference. It can be also concluded from **Fig. 8** (a) and (b) that for GPEH at the position 1.5*D* in the upstream and the position 0*D* at the throat, the distances from the bluff body to the low-pressure region are quite similar. This is because the low-pressure region also moves to the downstream direction while the bluff body is moving in the same direction. However, the difference in the pressure distribution between **Fig. 8** (a) and (b) reflects the fact that the vortex shedding in **Fig. 8** (a) is not as strong as that of **Fig. 8** (b).

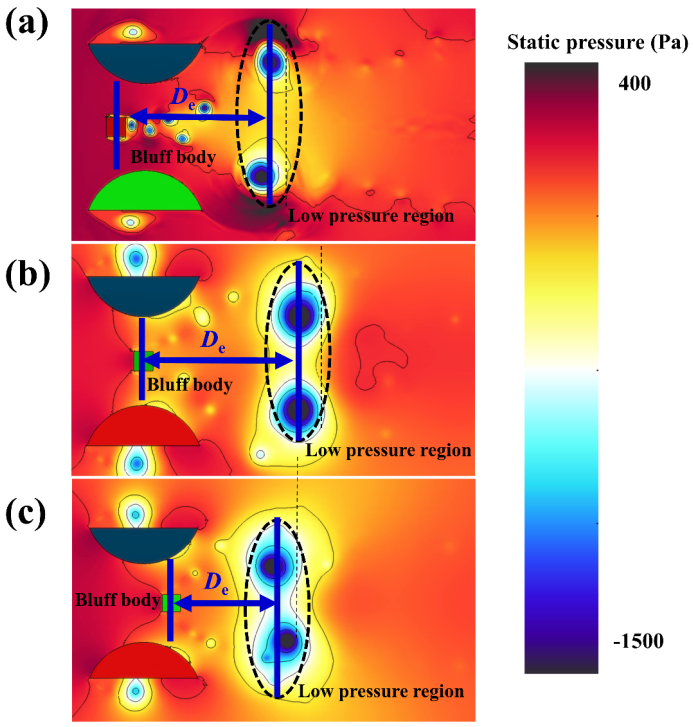


**Fig. 8** Comparisons of static pressure distribution: (a) position 1.5*D* (upstream), (b) position 0*D* (throat), and (c) position -1.5*D* (downstream).

As for the velocity variations, as shown in **Fig. 9**, it is obvious that the velocity difference of the position 0*D* at the throat is much greater than that at the position 1.5*D* upstream. This can reasonably explain why the case in **Fig. 8** (b) is underlying more severe aerodynamic force distribution. When the

GPEH is at the position $-1.5D$ in the downstream area, as shown in **Fig. 8** (c) and **Fig. 9** (c), the pressure distribution and the velocity iso-contour map are similar to that of the GPEH at position $0D$ (the throat). It can be seen from **Figs. 8** (b-c) that the effective distance ($D_e$) between the bluff body and the low-pressure region is much smaller at the position $-1.5D$ than that of $0D$. Meanwhile, in the position of the throat, the wind is already accelerated under the nozzle effect for configuration of -1.5$D$, thus, the wind besides the bluff body would also be accelerated. These two reasons may explain why the wake vortex shedding behind the bluff body grow larger and higher pressure-difference is formed in **Fig. 8** (c). In addition, it can also be noted that the spacing between the two symmetrical wake shedding vortices decreases by comparing the three cases shown in **Fig. 8**, which can also indicate that the flow effect on the bluff body in **Fig. 8** (c) due to that the low-speed areas is more concentrated. Thus, it can be summarized from the CFD results in **Figs. 7-9** that the downstream area is more favorable for GPEH performance enhancement, compared to the upstream area.

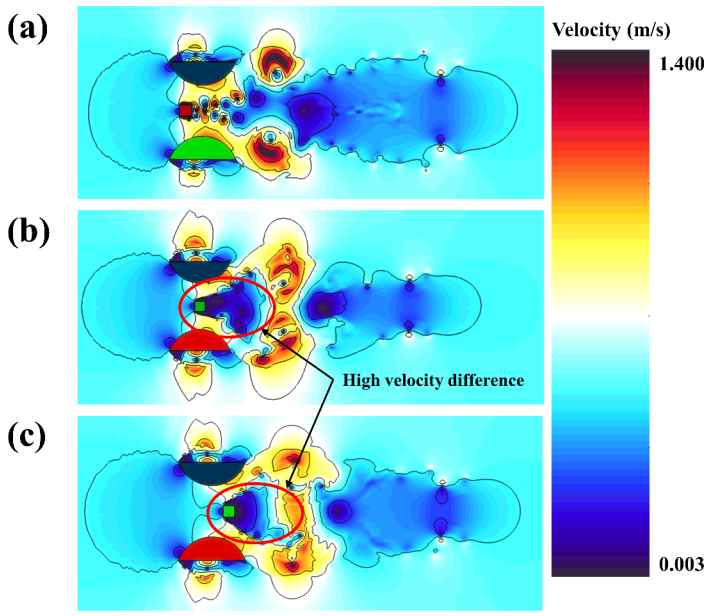


**Fig. 9** Comparisons of velocity iso-contour maps: (a) position 1.5 *D* (upstream), (b) position 0 *D* (throat), and (c) position -1.5 *D* (downstream).

## 5. Conclusions

This study proposed the concept of utilizing two half-cylinder obstacles for the performance enhancement of a galloping-based piezoelectric energy harvester (GPEH). A variable cross-section tube was formed by two half-cylinder obstacles and the GPEH placed in the tube. The experimental results show that the GPEH in the downstream area of the tube outperforms the GPEH in the upstream area of the tube and the device without the obstacles. The GPEH at the downstream positions -1.5$D$ and -2.5$D$ significantly outperform the cases in the other positions. When the GPEH is in the optimal configuration $L$ = -1.5$D$, compared with the traditional GPEH, the cut-in speed of the GPEH with the two half-cylinder obstacles is reduced by 43.87%, from 2.23 m/s to 1.55 m/s. For the highest experimental wind speed of 4.29 m/s, the output voltage of the GPEH with the two half-cylinder obstacles is increased by 109.28 %, from 4.31 V to 9.02 V. In addition, the experimental results have indicated that when the inlet wind speed is low ($U \leq 3.74$ m/s), the performance of the GPEH with the obstacles can be improved by increasing the obstacle curvature and reducing the throat width. The CFD simulations explained in a better way the physical effects of the obstacles on the vortex shedding around the GPEH. The results showed that when the GPEH is placed in the downstream area of the tube formed by the obstacles, a significant low-pressure region stays behind the bluff body due to the large vortex shedding. As a result, this low-pressure region significantly improves the vibration of the GPEH, leading to energy harvesting enhancement. Thus, the downstream area is beneficial to the GPEH, whereas the upstream area degrades the performance. It should be mentioned that the use of two half-cylinder obstacles changes the airflow around the GPEH, thereby significantly improving the performance of energy harvesting. This improvement is easy to control and can be applied to various types of GPEH structures, but this modification may increase additional costs due to oversize. Therefore, the focus of future research is to streamline the design of the structure and develop its application in various types of energy harvesters.

**Acknowledgement**

This work was supported by the National Natural Science Foundation of China (51977196 and 11802097), Open Fund of Science and Technology on Thermal Energy and Power Laboratory (TPL2019A01), SKL of HESS-2124, and China Postdoctoral Science Foundation (2020T130557).

**References**

1. Rashid, K., K. Mohammadi, and K. Powell, *Dynamic simulation and techno-economic analysis of a concentrated solar power (CSP) plant hybridized with both thermal energy storage and natural gas.* Journal of Cleaner Production, 2020. **248**.
2. Yang, K., et al., *High-resolution monitoring of aerospace structure using the bifurcation of a bistable nonlinear circuit with tunable potential-well depth.* Aerospace Science and Technology, 2019. **87**: p. 98-109.
3. Perveen, R., N. Kishor, and S.R. Mohanty, *Off-shore wind farm development: Present status and challenges.* Renewable & Sustainable Energy Reviews, 2014. **29**: p. 780-792.
4. Song, D., et al., *Power extraction efficiency optimization of horizontal-axis wind turbines through optimizing control parameters of yaw control systems using an intelligent method.* Applied energy, 2018. **224**: p. 267-279.
5. Fang, H., et al., *Industrial waste heat utilization for low temperature district heating.* Energy Policy, 2013. **62**(nov.): p. 236-246.
6. Zhu, H., G. Li, and J. Wang, *Flow-induced vibration of a circular cylinder with splitter plates placed upstream and downstream individually and simultaneously.* Applied Ocean Research, 2020. **97**: p. 102084.
7. Zhang, B., et al., *Numerical investigation on VIV energy harvesting of four cylinders in close staggered formation.* Ocean Engineering, 2018. **165**: p. 55-68.
8. Tang, L., et al., *Equivalent circuit representation and analysis of galloping-based wind energy harvesting.* IEEE/ASME Transactions on Mechatronics, 2014. **20**(2): p. 834-844.
9. Shi, M., A.S. Holmes, and E.M. Yeatman, *Piezoelectric wind velocity sensor based on the variation of galloping frequency with drag force.* Applied Physics Letters, 2020. **116**(26): p. 264101.
10. Elahi, H., et al., *Performance Evaluation of a Piezoelectric Energy Harvester Based on Flag-Flutter.* Micromachines, 2020. **11**(10): p. 933.
11. Zhou, Z., et al., *Scavenging wind energy by a dynamic-stable flutter energy harvester with rectangular wing.* Applied Physics Letters, 2019. **114**(24): p. 243902.
12. Abdelkefi, A., *Aeroelastic energy harvesting: A review.* International Journal of Engineering Science, 2016. **100**: p. 112-135.
13. Zhao, L.-C., et al., *Magnetic coupling and flextensional amplification mechanisms for high-robustness ambient wind energy harvesting.* Energy Conversion and Management, 2019. **201**: p. 112166.

14. Zhou, S. and L. Zuo, *Nonlinear dynamic analysis of asymmetric tristable energy harvesters for enhanced energy harvesting.* Communications in Nonlinear Science and Numerical Simulation, 2018. **61**: p. 271-284.
15. Fan, K., et al., *Hybridizing linear and nonlinear couplings for constructing two-degree-of-freedom electromagnetic energy harvesters.* International Journal of Energy Research, 2019. **43**(14): p. 8004-8019.
16. Chen, Z., et al., *Elastic-electro-mechanical modeling and analysis of piezoelectric metamaterial plate with a self-powered synchronized charge extraction circuit for vibration energy harvesting.* Mechanical Systems and Signal Processing, 2020. **143**: p. 106824.
17. Zhang, L., et al., *Galloping Triboelectric Nanogenerator for Energy Harvesting under Low Wind Speed.* Nano Energy, 2020. **70**: p. 104477.
18. Liu, H., et al., *Hybrid energy harvesting technology: From materials, structural design, system integration to applications.* Renewable and Sustainable Energy Reviews, 2020: p. 110473.
19. Shan, X.B., et al., *Enhancing the performance of an underwater piezoelectric energy harvester based on flow-induced vibration.* Energy, 2019. **172**: p. 134-140.
20. Wang, D.-A. and H.-H. Ko, *Piezoelectric energy harvesting from flow-induced vibration.* Journal of Micromechanics and Microengineering, 2010. **20**(2): p. 025019.
21. Abdelkefi, A., M.R. Hajj, and A.H. Nayfeh, *Power harvesting from transverse galloping of square cylinder.* Nonlinear Dynamics, 2012. **70**(2): p. 1355-1363.
22. Javed, U. and A. Abdelkefi, *Impacts of the aerodynamic force representation on the stability and performance of a galloping-based energy harvester.* Journal of Sound and Vibration, 2017. **400**: p. 213-226.
23. Wang, J., et al., *The state-of-the-art review on energy harvesting from flow-induced vibrations.* Applied Energy, 2020. **267**: p. 114902.
24. Zhao, L. and Y. Yang, *An impact-based broadband aeroelastic energy harvester for concurrent wind and base vibration energy harvesting.* Applied Energy, 2018. **212**: p. 233-243.
25. Sun, W., F. Guo, and J. Seok, *Development of a novel vibro-wind galloping energy harvester with high power density incorporated with a nested bluff-body structure.* Energy Conversion and Management, 2019. **197**: p. 111880.
26. Bibo, A., A.H. Alhadidi, and M.F. Daqaq, *Exploiting a nonlinear restoring force to improve the performance of flow energy harvesters.* Journal of Applied Physics, 2015. **117**(4): p. 045103.
27. Alhadidi, A.H. and M.F. Daqaq, *A broadband bi-stable flow energy harvester based on the wake-galloping phenomenon.* Applied Physics Letters, 2016. **109**(3): p. 033904.
28. Wang, J., et al., *Design, modeling and experiments of broadband tristable galloping piezoelectric energy harvester.* Acta Mechanica Sinica, 2019: p. in press.
29. Yang, K., J. Wang, and D. Yurchenko, *A double-beam piezo-magneto-elastic wind energy harvester for improving the galloping-based energy harvesting.* Applied Physics Letters, 2019. **115**(19): p. 193901.
30. Wang, J., et al., *Dynamics of the double-beam piezo-magneto-elastic nonlinear wind energy harvester exhibiting galloping-based vibration.* Nonlinear Dyn, 2020.
31. Zhao, L. and Y. Yang, *Comparison of four electrical interfacing circuits in wind energy harvesting.* Sensors and Actuators A: Physical, 2017. **261**: p. 117-129.
32. Lan, C., L. Tang, and R.L. Harne, *Comparative methods to assess harmonic response of nonlinear piezoelectric energy harvesters interfaced with AC and DC circuits.* Journal of Sound and Vibration, 2018. **421**: p. 61-78.

33. Kluger, J., F. Moon, and R. Rand, *Shape optimization of a blunt body vibro-wind galloping oscillator.* Journal of Fluids and Structures, 2013. **40**: p. 185-200.
34. Wang, J., et al., *Enhancement of low-speed piezoelectric wind energy harvesting by bluff body shapes: Spindle-like and butterfly-like cross-sections.* Aerospace Science and Technology, 2020: p. 105898.
35. Yang, K., et al., *Magnet-induced monostable nonlinearity for improving the VIV-galloping-coupled wind energy harvesting using combined cross-sectioned bluff body.* Smart Materials and Structures, 2020. **29**(7): p. 07lt01.
36. Wang, J., et al., *High-performance piezoelectric wind energy harvester with Y-shaped attachments.* Energy Conversion and Management, 2019. **181**: p. 645-652.
37. Hu, G., K.-T. Tse, and K.C. Kwok, *Enhanced performance of wind energy harvester by aerodynamic treatment of a square prism.* Applied Physics Letters, 2016. **108**(12): p. 123901.
38. Yang, Y., L. Zhao, and L. Tang, *Comparative study of tip cross-sections for efficient galloping energy harvesting.* Applied Physics Letters, 2013. **102**(6): p. 064105.
39. Wang, J.L., et al., *Hybrid wind energy scavenging by coupling vortex-induced vibrations and galloping.* Energy Conversion and Management, 2020. **213**: p. 112835.
40. Hu, G., et al., *Experimental investigation on the efficiency of circular cylinder-based wind energy harvester with different rod-shaped attachments.* Applied Energy, 2018. **226**: p. 682-689.
41. Abdelkefi, A., et al., *Performance enhancement of piezoelectric energy harvesters from wake galloping.* Applied Physics Letters, 2013. **103**(3): p. 033903.
42. Zhang, L.B., et al., *Improving the performance of aeroelastic energy harvesters by an interference cylinder.* Applied Physics Letters, 2017. **111**(7): p. 5.
43. Zhang, L.B., et al., *Experimental investigation of aerodynamic energy harvester with different interference cylinder cross-sections.* Energy, 2019. **167**: p. 970-981.
44. Wang, J., et al., *Enhancing energy harvesting from flow-induced vibrations of a circular cylinder using a downstream rectangular plate: An experimental study.* International Journal of Mechanical Sciences, 2021. **211**: p. 106781.
45. Yan, Z., et al., *Wind piezoelectric energy harvesting enhanced by elastic-interfered wake-induced vibration.* Energy Conversion and Management, 2021. **249**: p. 114820.
46. Fan, X., et al., *Experimental investigation on flow-induced vibration of flexible multi cylinders in atmospheric boundary layer.* International Journal of Mechanical Sciences, 2020. **183**: p. 105815.
47. Kaushik, M., *Theoretical and Experimental Aerodynamics*. 2019: Springer.
48. Hu, G., et al., *Performance evaluation of twin piezoelectric wind energy harvesters under mutual interference.* Applied Physics Letters, 2019. **115**(7): p. 073901.
49. Ramirez, J.M., *A coupled formulation of fluid-structure interaction and piezoelectricity for modeling a multi-body energy harvester from vortex-induced vibrations.* Energy Conversion and Management, 2021. **249**: p. 114852.
50. Kumar, N., et al., *A discrete linear stability analysis of two-dimensional laminar flow past a square cylinder.* WSEAS Transactions on Fluid Mechanics, 2021. **16**: p. 109-119.